Nanoscale Horizons

ROYAL SOCIETY OF CHEMISTRY

COMMUNICATION

View Article Online
View Journal | View Issue

Cite this: *Nanoscale Horiz.*, 2022, 7, 554

Received 16th January 2022,
Accepted 11th March 2022

DOI: 10.1039/d2nh00023g

rsc.li/nanoscale-horizons

Etched-spiky Au@Ag plasmonic-superstructure monolayer films for triple amplification of surface-enhanced Raman scattering signals†

Huiqin Liu,‡[ab] Junyi Zeng,‡[bc] Liping Song,*[ad] Lingli Zhang,[b] Zihai Chen,[e] Jianhua Li,[f] Zhidong Xiao,*[a] Fengmei Su[c] and Youju Huang*[b]

Generally, a high quality surface-enhanced Raman spectroscopy (SERS) substrate often requires a highly-tailorable electromagnetic (EM) field generated at nanoparticle (NP) surfaces by the regulation of the morphologies, components and roughness of NPs. However, most recent universal approaches are restricted to single components, and integrating these key factors into one system to achieve the theoretically maximum signal amplification is still challenging. Herein, we design a triple SERS signal amplification platform by the coordination of spiky Au NPs with rich-tip nanostructures, controllable silver nanoshell, as well as tailorable surface roughness into one nano-system. As a result, the theoretical electromagnetic field of the interfacial self-assembled 2D substrate can be improved by nearly 5 orders of magnitude, and the ideal tracing capability for the model SERS molecule can be achieved at levels of 5×10^{-11} M. Finally, diverse analytes in pesticide residues, environmental pollutants as well as medically diagnose down to 10^{-11} M and can be fingerprinted by the proposed SERS nano-platform. Our integrated triple amplification platform not only provides an effective SERS sensing strategy, but also makes it possible to simultaneously achieve high sensitivity, stability as well as universality into one plasmonic-based SERS sensing system.

New concepts

Herein, we demonstrate the triple surface-enhanced Raman spectroscopy (SERS) signal amplification platform by the design of the spiky Au NPs with rich tip nanostructures, controllable silver nanoshell, as well as tailorable surface roughness into one nano-system. As a result, the theoretical electromagnetic field of the interfacial self-assembled 2D SERS substrate can be improved by nearly 5 orders of magnitude, and the ideal tracing capability for diverse analytes in pesticide residues, environmental pollutants as well as medical diagnose can be achieved at levels of 5×10^{-11} M. This proposed SERS nano-platform provides approachable fabrication means for sensitive optical analysis technology, and is beneficial to the advances of multi-fields detection.

Introduction

Surface-enhanced Raman spectroscopy (SERS) as a non-invasive spectroscopy technique provides rapid, fingerprint identification of trace-molecule levels for all kinds of target analytes.[1,2] Since first put forward by Fleischmann in 1974,[3] the SERS technique has developed rapidly and widely in fields of chemical, physical and biological sciences.[4–6] However, the inherent Raman signals of most analyte molecules are weak due to their poor Raman scattering cross-sections.[7] In recent years, two dominant strategies involving electromagnetic (EM) mechanisms and chemical mechanisms have elaborated their vital importance for SERS enhancement.[8,9] Generally, the electromagnetic field is amplified ("hotspot effect") by noble metal NPs enabling numerous opportunities for tailoring the SERS detecting sensitivity, which is independent of the nature of analyte molecules.[10] In principle, the "hotspot density" of noble metal NPs has been adjusted broadly covering the design and selection of the morphology,[11,12]

[a] College of Science, Huazhong Agricultural University, Wuhan, 430070, China
[b] College of Material, Chemistry and Chemical Engineering, Key Laboratory of Organosilicon Chemistry and Material Technology, Ministry of Education, Hangzhou Normal University, Hangzhou, 311121, China. E-mail: yjhuang@hznu.edu.cn
[c] National Engineering Research Centre for Advanced Polymer Processing Technology, Zhengzhou University, Zhengzhou, 450002, China
[d] National Synchrotron Radiation Laboratory, CAS Key Laboratory of Soft Matter Chemistry, Anhui Provincial Engineering, Laboratory of Advanced Functional Polymer Film, University of Science and Technology of China, Hefei, 230026, China
[e] Anhui Shenghaitang Traditional Chinese Medicine Decoction Pieces Co., Ltd, Bozhou, 211 Zhangliang Road, Qiaocheng District, 236800, China
[f] Anhui Topway Testing Services Co.,Ltd, Xuancheng Economic and Technological Development Zone, 18 Rixin Road, 242000, China

† Electronic supplementary information (ESI) available. See DOI: 10.1039/d2nh00023g

‡ These authors contribute equally to this work.

composition[13,14] and roughness[15,16] of SERS substrates of NPs. It is worth noting that the SERS enhancement is highly dependent on the shape of metallic nanoparticles. The nanostructures with rich tips often exhibit unique advantages in concentrating the electromagnetic field, namely, the so-called "lightning rod effect".[17] The "lightning rod effect" is often caused by the curvature of a metallic interface induced by the potential gradient.[18] For instance, Fang and co-workers[19] synthesized flowerlike Au NPs with rich nanothorns by electrochemical deposition to achieve the SERS enhancement. Thus, the controllable fabrication of anisotropic nanostructures ranging from nanorods and nanotriangles to multi-branched metal NPs is conducive to SERS enhancement.[20,21]

Although the design of NPs with shape corners can partially circumvent the substrate limitation, the SERS enhancement is still weak on the surface of pure and single metal NPs.[22] Considering that, Tian's group puts forward versatile shell-isolated NP-enhanced Raman spectroscopy (SHINERS) technology by coating noble NPs with thin silica or alumina shells, in which the interaction with the chemical environment or analytical targets can be prevented.[23,24] Particularly, the sharp resonance characteristic of Ag nanostructures can effectively avoid self-adsorption and present high-scattering efficiency than Au NPs.[25,26] Thus, the "core–shell effect" of the complex structures of Au-Ag core–shell NPs, which distinguishes from SHINERS, can provide cooperative reinforcement for the SERS enhancement.[27,28] Furthermore, surface chemistry and roughness regulation for noble NP-based SERS substrate is another effective approach for optimizing SERS properties besides morphology tailoring. Generally, the surface roughness regulation involves controlled removal/addition of surface atoms from/on the NPs. Therefore, it creates more opportunities for some additional strong and homogeneous "hot spots" by leveraging the coupling between surface plasmons and far-field light.[29,30] The contribution of roughness (Nanocorrugation-Contributed Roughness, NCR) to SERS is further determined by the height of nanoripples or depth of grooves on a rough surface, which is named as "etching induced defect effect".[31] Despite the rapid advances of SERS detecting technology, the current strategies for SERS signal enhancement mainly focus on single or binary plasmonic nanostructure designs, which limits the maximum effect of SERS signal amplification. Thus, centralizing SERS enhancement factors into one nanostructure substrate to achieve theoretically maximum SERS magnification is still challenging.

In this work, we manage to integrate three key factors into one SERS nano-platform by tailoring the morphologies (holes and hotspots), composition and surface roughness of plasmonic substrates. Specifically, the integrated nanostructure is achieved by involving the systematic synthesis of spiky Au NPs with rich nano-tips, the spiky Au–Ag core–shell NPs with controllable thickness to the final etched spiky Au–Ag core–shell NPs with tailorable surface roughness (Fig. 1a). As a proof-of-concept, we utilize the Finite Difference Time Domain (FDTD) simulation to evaluate the electromagnetic enhancement of the integrating nanostructures, in which, the "integrated triple amplification" for SERS enhancement is verified. To estimate the sensing capabilities and versatility of our proposed integrated triple amplification SERS platform, we investigated the SERS-sensing properties for the model molecule (4-aminothiophenol, 4-ATP). In recent years, our group has devoted itself to constructing macroscopic and uniform NPs monolayer films[32,33] and investigated their functional applications for SERS detection.[34,35] Thus, leveraging interfacial assembly for obtaining scale-up and uniform 2D NP arrays, both sensitivity and stability are heightened in our 2D plasmonic SERS sensing platform (Fig. 1b). Finally, the integrated triple amplification SERS platform enables the effective detection of diverse molecules in pesticide residues, environmental pollutants as well as medical diagnose with strong quantitative capability down to 10^{-11} M (Fig. 1c). We envision that the proposed SERS platform not only achieves an integration of multiple signal amplification factors but also paves the way for wide-field trace analysis with high sensitivity and repeatability.

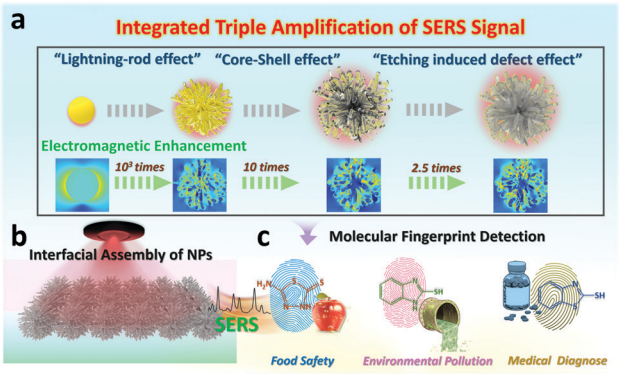

Fig. 1 Schematic illustration of the design of the integrated triple amplification of SERS signal: (a) structure design by tailoring the morphology, composition and surface roughness in one nanostructure for enhancing SERS detecting sensitivity; (b) interfacial assembly of the proposed nanostructures for enhancing SERS detection repeatability; (c) the application of the proposed triple amplification SERS nano-platform for real sample detection in various fields.

Materials

Chloroauric acid ($HAuCl_4 \cdot 3H_2O$, 99.0%), hexadecyl trimethyl ammonium bromide (CTAB, 99.0%), hexadecyl trimethyl ammonium chloride (CTAC, 99.0%), trisodium citrate dehydrate (SC, ≥99.0%), tris(hydroxymethyl)-amino-methane (TB, GR) were purchased from Sigma-Aldrich (USA). Ascorbic acid (AA, 99.7%), silver nitrate ($AgNO_3$, >99.0%), L-Cysteine (L-Cys, ≥98.5%), methanol, ethanol absolute, *n*-hexane (GR), 30.0% hydrogen peroxide (H_2O_2), 30.0% ammonium hydroxide (NH_4OH) were purchased from Sinopharm Chemical Reagent Co., Ltd (Shanghai, China). 4-Aminothiophenol (4-ATP, 97.0%) was obtained from Alfa Aesar (Shanghai, China). 5-Amino-2-thiol-1,3,4-thiadiazole (AMT, 98.0%), 2-mercaptobenzothiazole (2-MBT, 98.0%), 2-mercaptobenzimidazole (2-MBI, 98.0%) were purchased from Aladdin (Shanghai, China). All chemicals were used without further purification. Deionized water was used throughout the experiment process.

Au NPs with a diameter of 25 nm were prepared according to our reported method.[36] Typically, fresh $HAuCl_4$ (1 mL, 25 mM)

and TB (5 mL, 0.1 M) were sequentially added (time delay 60 s) to 140 mL of boiling deionized water containing 2.2 mM SC, and the reaction was allowed to proceed at 137 °C for 15 min under stirring. Afterward, the solution was cooled down to 100 °C and 1 mL of $HAuCl_4$ (25 mM) was injected twice into the solution with an interval of 20 min.

The spiky Au NPs were prepared according to a previously reported method with some modifications.[37] 16 mL of 0.1 M CTAB and 1.6 mL of 25 mM fresh HAuCl4 were sequentially added to 79 mL of deionized water under stirring. Then, AA solution (9.5 mL, 0.1 M), L-Cys (0.5 mL, 1 mM) and as-synthesized Au NPs (1 mL, 30 nm) were sequentially added (time delay 30 s) under water bath at 30 °C for 2 h. The solution was purified by centrifugation three times at 4000 rpm and dispersed in 60 mL of 1 mM CTAB solution.

The spiky Au@Ag NPs were prepared according to our reported method with some modifications.[38] 50 μL of 0.01 M $AgNO_3$ solution was added to 5 mL of the 80 mM CTAC-modified spiky Au NPs under ultrasonic conditions. After 30 s, AA (100 μL, 0.1 M) solution was added with successive ultrasound for 1 min. Then, the tube was placed in a water bath at 65 °C for 4 h. Finally, the product was washed three times with distilled water and dispersed in 1 mM CTAC solution. By changing the volume of $AgNO_3$ and AA, the spiky Au@Ag NPs with different thicknesses were obtained.

Monolayer films of Au NPs, spiky Au NPs and spiky Au@Ag NPs were prepared according to our previous interfacial assembly approach with some modifications.[36] The freshly prepared Au NP solution (8 mL) was diluted with 2 mL of deionized water and the mixture solution was added to a glass culture dish (6 cm in diameter). Then, 8 mL of hexane was slowly, dropwise, added on top of the solution to form an incompatible oil–water interface. Finally, 10 mL of ethanol was added to an aqueous solution with a mechanical injection pump at a constant rate of 3 mm min^{-1} to form monolayer film at the interface. Typically, the spiky Au NPs and spiky Au@Ag NP monolayer films were prepared using the same method mentioned above for Au NPs. Furthermore, the NP monolayer films were transferred to a Si–wafer substrate for further use.

Etching for the spiky Au@Ag NP monolayer film was according to a previously reported method with some modifications.[39] 30% H_2O_2, 30% NH_4OH and methanol were mixed in a volume ratio of 1 : 1 : 4 as an aqueous etchant. The spiky Au@Ag NP monolayer films were immersed in 1 mL aqueous etchant for 0, 20, 40, 60, 80, 100 and 120 s, respectively. The substrates were immediately immersed in deionized water to extinguish the etching reaction. Finally, the etched substrates were washed three times with deionized water and dried at room temperature.

Finite-difference time-domain (FDTD) solutions 8.24 (Lumerical Solutions) was applied to FDTD simulations. Notably, an electromagnetic pulse from 400 nm to 1000 nm, in which the electric field perpendicular was to the substrate, was launched into the simulated domain with nanostructures. A mesh size of 0.1 nm was employed for acquiring the electric field contours of Au NPs. The models of other nanostructures with the grid accuracy of 0.5 nm were simplified based on real morphologies from TEM and SEM results. The average NP sizes of Au NPs, spiky Au NPs as well as the thickness of silver nanoshells were determined as 31 nm, 200 nm and 2.5 nm, respectively. The refractive index of the surrounding medium of water was set to be 1.33. The dielectric functions of Au and Ag were obtained by fitting the measured data of Johnson and Christy.

The Si–wafer-supported Au NPs, spiky Au NPs, spiky Au@Ag NPs and etched spiky Au@Ag NP monolayer films were immersed in 4-ATP ethanol solution for 24 h and then rinsed repeatedly with ethanol to remove any surface residue.

To verify the practical applicability of the etched spiky Au@Ag NP monolayer films in different fields, we applied it to SERS detection of real samples including food safety, environmental pollution and medical diagnosis. Different concentrations of AMT, 2-MBI and 2-MBT were added to vegetables, river water and urine for SERS measurement. We dropped 2 mL of AMT solution with different concentrations on 1 × 1 cm^2 squares of cabbage leaves and washed them repeatedly with 2 mL of water and DMF-mixed solution after drying. The river water and urine samples were diluted 100 times to avoid the background interference of impurities on the SERS signal.

UV-vis absorption spectra were obtained using a TU-1810 UV-vis spectrophotometer (Purkinje General Instrument Co, China). The SEM images were obtained on an S-4800 instrument (Hitachi, Japan) at an acceleration voltage of 8 kV. The TEM images are obtained by the JEM-2100F instrument ((JEOM, Japan)) at an accelerating voltage of 200 kV. SERS mapping images were obtained using an R-3000HR spectrometer (Renishaw, UK) with a 785 nm laser and 20× objective lens. The Raman scattering signals were recorded on an ATR8300-Raman spectrometer (OPTOSKY, China) with a 785 nm laser and 20× objective lens.

Results and discussion

Generally, the spiky Au NPs with an average size of 200 ± 25 nm were synthesized according to our previous work with minor modifications.[36] In the process of fabricating spiky Au NPs, the seeds of spherical Au NPs with an average size of 35 nm[37] (Fig. 2a and e) are added into the growth solution containing L-cysteine (L-Cys) with optimized amounts. Considering the outstanding electromagnetic coupling performance of multi-branched NPs, the relatively low coverage of L-Cys on Au NPs is necessary for obtaining uniform spiky Au NPs. As a result, the number of branches and SERS performance exhibits high dependence on the amount of L-Cys (Fig. S1 and S2, ESI†) and the average number of branches in the spiky Au NPs is approximately 20–30 per nanoparticle (Fig. 2c and g). Notably, the morphologies and optical properties of the spiky Au@Ag NPs exhibit strong seed size dependence (Fig. S3, ESI†). When the size of Au NPs seed was too small (Fig. S3a, ESI† 15 nm), the branches are obviously not shaped. Upon increasing the size of Au NPs seed to 25 nm, the spiky Au NPs with rich branches are formed (Fig. S3b, ESI†). However, by further increasing the size

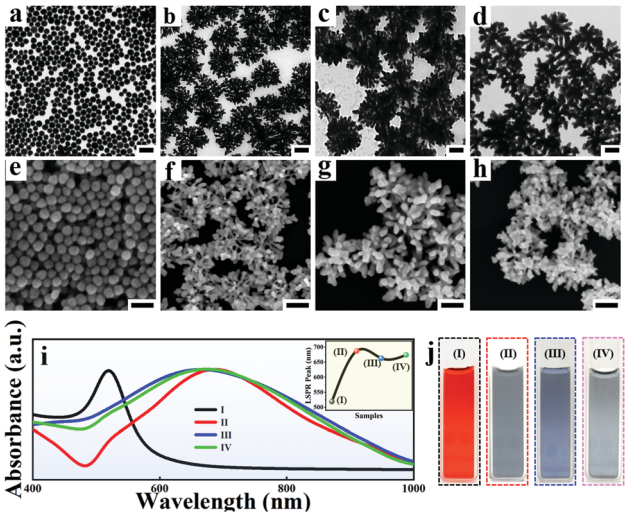

Fig. 2 TEM and SEM images of Au NPs (a and e), spiky AuNPs (b and f), spiky Au@Ag NPs (c and g) and etched-spiky Au@Ag NPs (d and g). (i and j) UV-vis spectra and optical photographs of the aqueous solution of Au NPs (I), spiky AuNPs (II), spiky Au@Ag NPs (III) and etched-spiky Au@Ag NPs (IV) (inset: LSPR peak location of the proposed four different NPs). The scale bar is 50 nm.

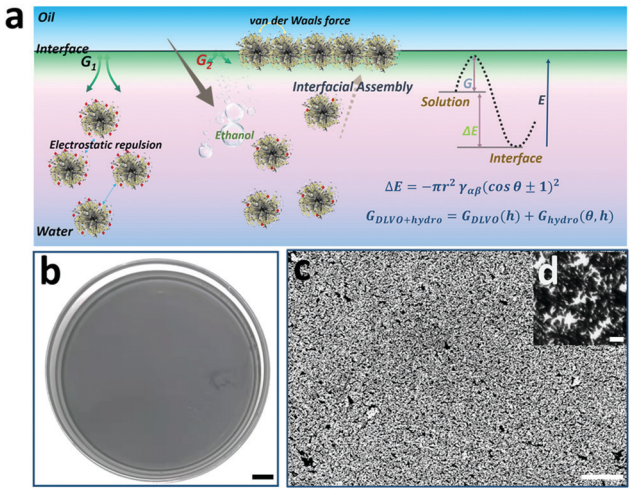

Fig. 3 (a) Schematic illustration of spiky Au@Ag NP monolayer films acquired at the oil–water interface. Optical photograph (b), SEM (c) and TEM (d) images of spiky Au@Ag NPs monolayer film. The scale bar is 1 cm (b), 20 μm (c) and 100 nm (d), respectively.

of Au NP seed to 50 nm, the branches became sharp and deformed (Fig. S3c, ESI†). Additionally, the spiky Au@Ag NPs were prepared and tailored according to the distinguished chemical wet method.[35] The TEM images (Fig. S4, ESI†), energy dispersive spectroscopy (Fig. S5, ESI†), as well as gradually blue-shifted UV-vis absorption spectrum (Fig. S6a and b, ESI†) indicate the successful coating of Ag nanoshells on the spiky Au NPs. Additionally, the thickness of Ag nanoshells (Fig. S6c, ESI†) was finely tuned with the size of 2 to 35 nm by simply varying the amount of $AgNO_3$ and AA in the growth process. Additionally, the Ag shell is optimized by evaluating the influence of different conditions for preparing an adjustable Ag shell on SERS performance (Fig. S7, ESI†).

Furthermore, the preciously-controllable etching on spiky Au@Ag NPs was conducted according to the typical selective chemical etching (Fig. 2d and h).[39] Considering the precise maneuverability for regulating the surface roughness of NPs, the aqueous etchant composed of 30% H_2O_2, 30% NH_4OH and methanol were chosen and the etched spiky Au@Ag NPs with different degrees of surface chemistry and roughness were obtained by simply tailoring the etching time. As shown in Fig. S8 (ESI†), the spectral and high definitude SEM characterization has proved the successful etching for spiky Au@Ag NPs. Finally, the UV-vis absorption spectrum up to 155 nm shifts (the inset picture of Fig. 2i) and color changes of four NPs (Fig. 2j) further confirmed the successful synthesis of the designed triple amplification SERS nano-platform. Additionally, similar to the Ag shell coating procedure, the etching for spiky Au@Ag NPs was optimized by evaluating the influence of different conditions for etching on SERS performance (Fig. S9 and S10, ESI†). The optimized etching time for the SERS enhancement of the etched spiky Au@Ag NPs was determined as 40 s (Fig. S10, ESI†).

Interfacial assembly of NPs at the water-oil interface has been a versatile approach for obtaining uniform and scale-up 2D NP arrays.[40] Especially, the ethanol injection method is most widely used due to its high accessibility and repeatability.[41] Considering the high-quality hot spot coupling in 2D NP arrays compared to that of dissociative ones,[42] interfacial assembly of spiky Au@Ag NPs was conducted to obtain highly strong and uniform electromagnetic coupling. As shown in Fig. 3a, the monodisperse spiky Au@Ag NPs are assembled into a scale-up monolayer film at the water/hexane interface by controllably injecting ethanol into Au@Ag NP solution. Considering the key role of ethanol in decreasing the kinetic adsorption barrier (ΔG),[43] the assembly area and uniformity of 2D monolayer films are controllable by tailoring the amount and injecting rate of ethanol in the solution. As shown in Fig. 3b, the macroscopic and uniform "grey film" is visible, and the assembly area is as large as 50 cm^2. Additionally, the SEM image of the 2D spiky Au@Ag NP arrays also demonstrates the high uniformity of 2D spiky Au@Ag NP arrays (Fig. 3c). The average distance between branches of closely arranged adjacent NPs in the monolayer film is determined to be 4.4 nm measured using Nano Measurer Software statistics (Fig. S11, ESI†). This is located in the range of optimized distances (1–5 nm) for maximized electromagnetic enhancement reported in previous work.[44] As shown in Fig. S12 (ESI†), both Au NPs and spiky Au NPs exhibit uniform SERS performance. Thus, we believe that the optimized NP monographs and density NP arrangement in the proposed 2D SERS nano-platform are all advantageous for SERS detection.

As proof-of-concept demonstrations, the logarithmic-scale electric field intensity enhancement contours were obtained by the FDTD calculations to evaluate the SERS enhancement factor of the proposed etched spiky Au@Ag NPs nano-platform, as shown in Fig. 4a. Notably, the spines on the spiky Au NPs grow asymmetrically during the synthesis procedure, which determines the structure asymmetry in the final etched spiky Au@Ag NPs.

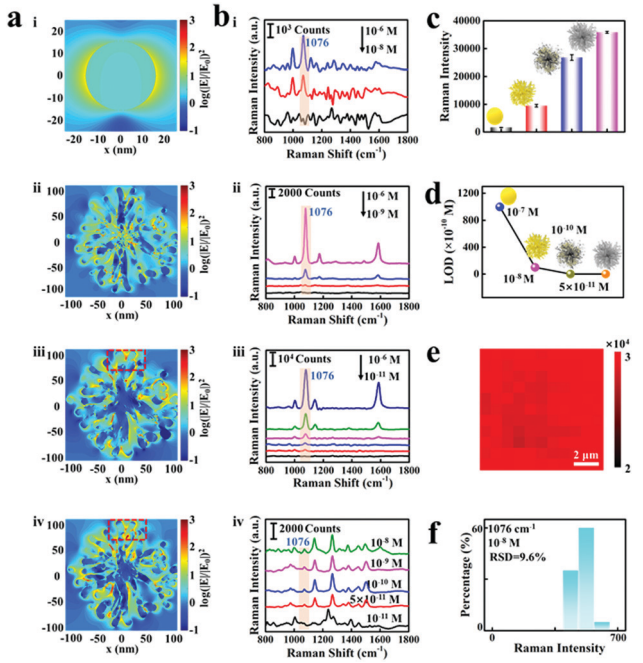

Fig. 4 Evaluation of SERS signal and electromagnetic field amplification for the proposed four different NPs. (a) FDTD simulation of the electric field distribution in the *xz*-plane for Au NP (i), spiky Au NP (ii), spiky Au@Ag NP (iii) and etched spiky Au@Ag NP (iv). (b) SERS spectra of 4-ATP on the Au NPs (i), spiky Au NPs (ii), spiky Au@Ag NPs (iii) and etched spiky Au@Ag NPs (iv) monolayer films. (c) Average Raman intensities at 1076 cm^{-1} peak of 4-ATP (10^{-6} M) on the proposed four NPs monolayer films. (d) The limit of detection (LOD) of 4-ATP on the proposed four NPs monolayer films. (e) SERS intensity mapping images of 4-ATP (10^{-6} M) measured at the 1076 cm^{-1} peak across a 10 × 10 μm^2 piece with 2 μm interval of the etched spiky Au@Ag NPs monolayer films. (f) Histogram of Raman signal intensity at 1076 cm^{-1} of 4-ATP at the concentration of 10^{-8} M on the etched spiky Au@Ag NP monolayer films.

The electromagnetic enhancement contours are calculated under the excitation at their corresponding dipolar plasmon wavelengths (i: 523 nm, ii: 687 nm, iii: 669 nm, iv: 700 nm). The spiky Au NPs exhibit obvious electromagnetic enhancement of 3 orders of magnitude compared to that in Au NPs (Fig. 4a-ii). This is reasonable because of the rich hot spot in nanogaps generated by the so-called "lightning-rod effect".[45] Additionally, the spiky Au@Ag NPs with 2.5 nm Ag nanoshells and etched spiky Au@Ag NPs show more than 4 orders of magnitude electromagnetic enhancement compared to that of Au NPs.

Furthermore, 4-ATP is chosen as a probing molecule to verify the triple SERS amplification effect of the proposed etched spiky Au@Ag NPs-SERS platform. The Au NPs, spiky Au NPs, spiky Au@Ag NPs and etched spiky Au@Ag NPs are interfacially assembled into 2D monolayer films for SERS detection. As reported previously,[42] the typical characteristic peaks of 4-ATP located at 1076, 1172, and 1578 cm^{-1} are apparent on these four NPs SERS substrates (Fig. 4b), which correspond to the mixed modes of C–C stretching, C–H bending vibration, as well as C–C stretching vibration, respectively. It is worth noting that the detecting limits of four different substrates involving Au NPs, spiky Au NPs, spiky Au@Ag NPs and etched spiky Au@Ag NPs are 10^{-7} M (ii), 10^{-8} M, 10^{-10} M (iii) and 5×10^{-11} M (iv), respectively. Generally, the SERS enhancement of spiky Au NPs exhibits a close correlation to the morphologies of spiky Au NPs, as shown in Fig. S4 (ESI†). Additionally, the SERS enhancement exhibits high dependence on the thickness of Ag nanoshells on spiky Au NPs and the optimized Ag nanoshell of 2.5 nm presents outstanding SERS performance, as shown in Fig. S3c (ESI†). Furthermore, the EF of the films can be calculated using the following equation:

$$EF = (I_{SERS} / N_{SERS})/(I_{NR} / N_{NR}) \quad (1)$$

where N_{NR} and N_{SERS} represent the number of 4-ATP molecules in the bulk solid sample and on the surface of the etched spiky Au@Ag NPs monolayer films; and INR and ISERS express the Raman scattering intensities from the solid 4-ATP and the 4-ATP adsorbed on the surface of the etched spiky Au@Ag NPs monolayer films.[36]

The EF is calculated to be 5.5×10^4 (Section S2 in ESI†), indicating the excellent SERS enhancement performance of the proposed triple signal amplification nano-platform. Thus, the designed triple signal amplification properties are evidenced (Fig. 4c) and the optimized etched spiky Au@Ag NPs exhibit high sensitivity for fingerprinting 4-ATP with concentrations down to 5×10^{-11} M (Fig. 4d).

Notably, not only high sensitivity but the 2D etched spiky Au@Ag NP arrays also exhibit high signal reproducibility, as shown in Fig. 4e. Each pixel at the spatial position of the SERS mapping images symbolizes the Raman intensity of 4-ATP at 1076 cm^{-1}. Confocal Raman images for 4-ATP signals at 1076 cm^{-1} from etched spiky Au@Ag NP monolayer films are shown in Fig. S13 (ESI†). The uniform red color of the mapping image indicates high reproducibility of the substrate even in a sharp SERS spectrum intensity range compared to previous work.[46] Although the distribution of hot spots in etched spiky Au@Ag NPs exhibits some heterogeneity (Fig. 4a), the construction of 2D monolayer films, in which NPs are arranged regularly and closely, further ensures the detection of uniformity of hot spots on the proposed SERS nano-platform. Additionally, in order to further explore the reproducibility of the substrate in low density analytical molecular detection, we plotted the histogram of Raman signal intensity at 1076 cm^{-1} of 4-ATP at the concentration of 10^{-8} M (Fig. 4f). The relative standard deviation (RSD) of the Raman signal of 4-ATP with different concentrations (10^{-6}, 10^{-8}, 10^{-10} M) is evaluated by randomly selecting 20 locations on the monolayer film of etched spiky Au@Ag NPs. In addition, the histogram distribution of these samples exhibited a lognormal curve distribution, which revealed the low relative standard deviation (Fig. S14, ESI†). These results demonstrate the good reproducibility for low-density analyte molecular detection.

Generally, the SERS detection for probing molecule has sufficiently verified the ultrahigh sensitivity, good reproducibility and excellent stability of the proposed triple amplified SERS nano-platform. Furthermore, the sensitive detection of real samples in three kinds of fields are systematically investigated, respectively. Here, three typical molecules ranging from food safety, environmental pollution as well as medical diagnosis are

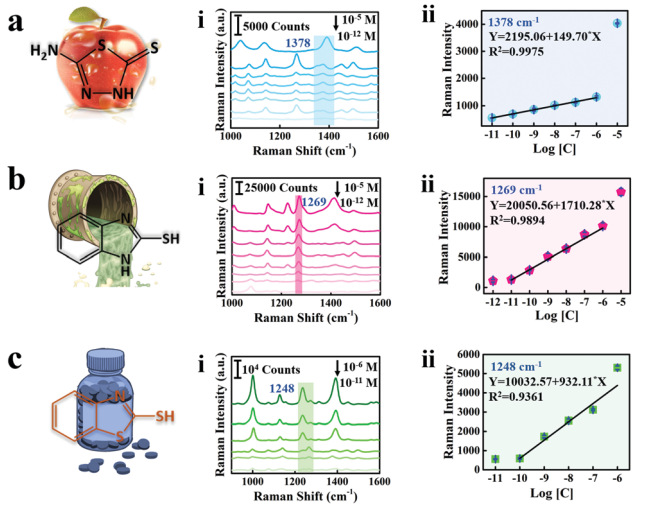

Fig. 5 The detection of various analytes in real samples on the etched spiky Au@Ag NP monolayer films. (a) Food safety: (i) SERS spectra of AMT at different concentrations. (ii) The relationship between the SERS intensity of the 1378 cm^{-1} peak and concentration of AMT. (b) Environmental pollution: (i) SERS spectra of 2-MBI at different concentrations. (ii) The relationship between the SERS intensity of the 1269 cm^{-1} peak and concentration of 2-MBI. (c) Medical diagnosis: (i) SERS spectra of 2-MBT at different concentrations. (ii) The relationship between the SERS intensity of the 1248 cm−1 peak and concentration of 2-MBT.

chosen as target analytes Among them, thiadiazole–copper as broad-spectrum microbicide has been widely used in the protection of crop pests. Thus, it is crucial for quantitative detection of pesticide residues [2-amino-5-mercapto-1,3,4-thiadiazole] (AMT).[47] Additionally, 2-mercaptobenzimidazole (2-MBI), which is widely applied in the industry as a rubber preservative, antioxidant and metal inhibitor, is of great significance to achieve ultrasensitive detection for 2-MBI.[48] 2-mercaptobenzothiazole (2-MBT) is a genotoxic impurity introduced by the cefotaxime sodium in the process of production and belongs to class 2A carcinogens in the list of carcinogens published by the World Health Organization International Research on Cancer.[49] It is a great promise for 2-MBT detection in urine in the monitoring of drug quality and medical health. In this work, in order to achieve sensitive monitoring of those typical molecules, AMT was dissolved in a solution composed of DMF and H_2O in the ratio of 2 : 1 by volume and 2-MBI and 2-MBT were dissolved in ethanol. In addition, they are configured into standard solutions with different concentrations for SERS detection (Fig. S15, ESI†). The results demonstrate the high university of the proposed triple amplified SERS nano-platform for tracing analytes with fingerprinting levels.

As shown in Fig. 5, the SERS spectra and linear calibration plot of different concentrations of AMT, 2-MBI, and 2-MBT are presented and the characteristic peaks of the analyte molecule are marked with a band in Fig. 5a(i)–c(i). The characteristic bands at 1378 cm^{-1}, 1269 cm^{-1} and 1248 cm^{-1} are significant and selected as the standard peaks of AMT, 2-MBI and 2-MBT for quantitative analysis. Generally, the peak located at 1378 cm^{-1} corresponds to the C_5–N_4 stretching of AMT,[50] 1269 cm^{-1} corresponds to the mixed modes of C=N, C–C stretching and C–H bending vibration of 2-MBI[51] and 1248 cm^{-1} corresponding to the C=N–C bending vibration of 2-MBT.[52] Therefore, the Raman intensity increases with the increase of analyte molecule concentrations. Furthermore, the linear calibration plots between the SERS intensity and analyte molecule concentration are shown in Fig. 5a(ii)–c(ii). The limit of detection (LOD) of AMT residues on cabbage leaves is 2.13×10^{-5} mg kg^{-1},[53] which is much lower than those from maximum residue limits (MRL) in China and the European Union (Table S1, ESI†). Thus, we fully believe that the proposed triple amplified SERS nano-platform can perform ultra-sensitive detection for real samples and has potential application value for practical detection.

Conclusions

In this work, we have successfully achieved the construction of a triple amplified SERS nano-platform by adjusting the structure, composition and surface chemistry and roughness in one nanostructure of etched spiky Au@Ag NPs. Then, as a proof-of-concept demonstration, the FDTD simulation of the proposed triple amplified SERS nano-platform exhibits strong electromagnetic enhancement nearly 10^5 times. Additionally, the detection sensitivity of the proposed triple amplified SERS nano-platform for probing molecules also shows four orders of magnitude enhancement compared to that of spherical Au NPs. Finally, the optimized triple-amplified SERS nano-platform is applied to real samples of food safety, aqueous environment detection and medical diagnosis with ultra-sensitive quantitative detection (10^{-11} M). We expect that the proposed triple amplified SERS nano-platform not only can contribute to further study of sensitive optical analysis technology but also be beneficial to the advances of multi-fields detection with balanced sensitivity and reproducibility.

Author contributions

Liping Song, Zhidong Xiao and Youju Huang designed the project; Huiqin Liu and Lingli Zhang conducted the relative experiment including synthesis of nanostructure, characterization, the preparation of monolayer films and SERS detection; Junyi Zeng conducted the FDTD simulation. Youju Huang, Zihai Chen, Jianhua Li and Fengmei Su analysis and discuss the results. Huiqin Liu and Liping Song draft the manuscript. Liping Song, Zhidong Xiao and Youju Huang revised the manuscript.

Conflicts of interest

There are no conflicts to declare.

Acknowledgements

We gratefully acknowledge the financial supports from the National Natural Science Foundation of China (51873222, 52111530128 and 52103325), the Zhejiang Provincial Natural Science Foundation of China (Z22B050001), Science and

Technology Innovation Project in Hubei Province (2021ACB001), the Fundamental Research Funds for Central Universities (2662019PY024), the Key Research and Development Projects of Anhui Province (202004g01020016 and 202104g01020009), the start-up funding from Hangzhou Normal University (4095C5021920452).

Notes and references

1 H. K. Lee, Y. H. Lee, C. S. L. Koh, G. C. Phan-Quang, X. Han, C. L. Lay, H. Y. F. Sim, Y. C. Kao, Q. An and X. Y. Ling, *Chem. Soc. Rev.*, 2019, **48**, 731–756.
2 C. Zong, M. Xu, L. J. Xu, T. Wei, X. Ma, X. S. Zheng, R. Hu and B. Ren, *Chem. Rev.*, 2018, **118**, 4946–4980.
3 J. Langer, D. J. de Aberasturi, J. Aizpurua, R. A. Alvarez-Puebla, B. Auguie, J. J. Baumberg, G. C. Bazan, S. E. J. Bell, A. Boisen, A. G. Brolo, J. Choo, D. Cialla-May, V. Deckert, L. Fabris, K. Faulds, F. J. G. de Abajo, R. Goodacre, D. Graham, A. J. Haes and C. L. Haynes, *ACS Nano*, 2020, **14**, 28–117.
4 W. Lee, B. H. Kang, H. Yang, M. Park, J. H. Kwak, T. Chung, Y. Jeong, B. K. Kim and K. H. Jeong, *Nat. Commun.*, 2021, **12**, 159.
5 J. Chen, G. Liu, Y. Z. Zhu, M. Su, P. Yin, X. J. Wu, Q. Lu, C. Tan, M. Zhao, Z. Liu, W. Yang, H. Li, G. H. Nam, L. Zhang, Z. Chen, X. Huang, P. M. Radjenovic, W. Huang, Z. Q. Tian, J. F. Li and H. Zhang, *J. Am. Chem. Soc.*, 2020, **142**, 7161–7167.
6 J. Chen, Y. Huang, P. Kannan, L. Zhang, Z. Lin, J. Zhang, T. Chen and L. Guo, *Anal. Chem.*, 2016, **88**, 2149–2155.
7 T. Tian, J. Yi, Y. Liu, B. Li, Y. Liu, L. Qiao, K. Zhang and B. Liu, *Biosens. Bioelectron.*, 2021, **197**, 113778.
8 S. E. J. Bell, G. Charron, E. Cortes, J. Kneipp, M. L. de la Chapelle, J. Langer, M. Prochazka, V. Tran and S. Schlucker, *Angew. Chem., Int. Ed.*, 2020, **59**, 5454–5462.
9 D. Kim, J. Kim, J. Henzie, Y. Ko, H. Lim, G. Kwon, J. Na, H. J. Kim, Y. Yamauchi and J. You, *Chem. Eng. J.*, 2021, **49**, 129445.
10 S. Y. Ding, E. M. You, Z. Q. Tian and M. Moskovits, *Chem. Soc. Rev.*, 2017, **46**, 4042–4076.
11 J. Fang, S. Du, S. Lebedkin, Z. Li, R. Kruk, M. Kappes and H. Hahn, *Nano Lett.*, 2010, **10**, 5006–5013.
12 B. Zhao, R. Hao, Z. Wang, H. J. Zhang, Y. W. Hao, C. Y. Zhang and Y. Q. Liu, *Chem. Eng. J.*, 2018, **349**, 581–587.
13 L. Zhou, J. Zhou, W. Lai, X. Yang, J. Meng, L. Su, C. Gu, T. Jiang, E. Y. B. Pun, L. Shao, L. Petti, X. W. Sun, Z. Jia, Q. Li, J. Han and P. Mormile, *Nat. Commun.*, 2020, **11**, 1785.
14 Y. F. Pang, J. M. Shi, X. S. Yang, C. W. Wang, Z. W. Sun and R. Xiao, *Biosens. Bioelectron.*, 2020, **148**, 111800.
15 H. Li, Q. Yang, J. Hou, Y. Li, M. Li and Y. Song, *Adv. Funct. Mater.*, 2018, **28**, 1800448.
16 Y. Li, L. Yu, J. S. Li, L. J. Wang and R. Lu, *Chem. Eng. J.*, 2020, **397**, 125434.
17 S. Go, S. Yoo, J. Son, S. Lee, J. Lee, S. Lee, J. Kim, M. Park, W. Park, J. M. Kim, J. M. Nam and S. Park, *Nano Lett.*, 2022, **22**, 1734–1740.
18 Y. Sun and Y. Xia, *Adv. Mater.*, 2003, **15**, 695–699.
19 L. Zhang, R. Hao, D. Zhang, H. You, Y. Dai, W. Liu and J. Fang, *Anal. Chem.*, 2020, **92**, 9838–9846.
20 M. C.-P. Leonardo Scarabelli, J. J. Giner-Casares, J. Langer and L. M. Liz-Marzán, *ACS Nano*, 2014, **8**, 5833–5842.
21 H. Chen, Z. Sun, W. Ni, K. C. Woo, H. Q. Lin, L. Sun, C. Yan and J. Wang, *Small*, 2009, **5**, 2111–2119.
22 J. F. Li, Y. J. Zhang, S. Y. Ding, R. Panneerselvam and Z. Q. Tian, *Chem. Rev.*, 2017, **117**, 5002–5069.
23 S. Y. Ding, J. Yi, J. F. Li, B. Ren, D. Y. Wu, R. Panneerselvam and Z. Q. Tian, *Nat. Rev. Mater.*, 2016, 1.
24 H. Zhang, C. Wang, H. L. Sun, G. Fu, S. Chen, Y. J. Zhang, B. H. Chen, J. R. Anema, Z. L. Yang, J. F. Li and Z. Q. Tian, *Nat. Commun.*, 2017, **8**, 15447.
25 W. Shen, X. Lin, C. Jiang, C. Li, H. Lin, J. Huang, S. Wang, G. Liu, X. Yan, Q. Zhong and B. Ren, *Angew. Chem., Int. Ed.*, 2015, **54**, 7308–7312.
26 J. Song, B. Duan, C. Wang, J. Zhou, L. Pu, Z. Fang, P. Wang, T. T. Lim and H. Duan, *J. Am. Chem. Soc.*, 2014, **136**, 6838–6841.
27 D. K. Lim, K. S. Jeon, H. M. Kim, J. M. Nam and Y. D. Suh, *Nat. Mater.*, 2010, **9**, 60–67.
28 L. Dai, L. Song, Y. Huang, L. Zhang, X. Lu, J. Zhang and T. Chen, *Langmuir*, 2017, **33**, 5378–5384.
29 M. S. Goh, Y. H. Lee, S. Pedireddy, I. Y. Phang, W. W. Tjiu, J. M. Tan and X. Y. Ling, *Langmuir*, 2012, **28**, 14441–14449.
30 H.-Y. Hsieh, J.-L. Xiao, C.-H. Lee, T.-W. Huang, C.-S. Yang, P.-C. Wang and F.-G. Tseng, *J. Phys. Chem. C*, 2011, **115**, 16258–16267.
31 H.-Y. Hsieh, J.-L. Xiao, C.-H. Lee, T.-W. Huang, C.-S. Yang, P.-C. Wang and F.-G. Tseng, *J. Phys. Chem. C*, 2011, **115**, 16258–16267.
32 L. P. Song, B. B. Xu, Q. Cheng, X. Y. Wang, X. N. Luo, X. Chen, T. Chen and Y. J. Huang, *Sci. Adv.*, 2021, **21**, 2852.
33 H. Lin, L. P. Song, Y. J. Huang, Q. Cheng, Y. P. Yang, Z. Y. Guo, F. M. Su and T. Chen, *ACS Appl. Mater. Interfaces*, 2020, **12**, 11296–11304.
34 L. P. Song, Y. J. Huang, Z. H. Nie and T. Chen, *Nanoscale*, 2020, **12**, 7433–7460.
35 L. P. Song, J. Cheng, B. B. Xu and Y. J. Huang, *ACS Nano*, 2021, **15**, 18822–18847.
36 X. F. Lu, Y. J. Huang, B. Q. Liu, L. Zhang, L. P. Song, J. W. Zhang, A. F. Zhang and T. Chen, *Chem. Mater.*, 2018, **30**, 1989–1997.
37 H. E. Lee, H. Y. Ahn, J. Mun, Y. Y. Lee, M. Kim, N. H. Cho, K. Chang, W. S. Kim, J. Rho and K. T. Nam, *Nature*, 2018, **556**, 360–365.
38 Y. Yang, L. Song, Y. Huang, K. Chen, Q. Cheng, H. Lin, P. Xiao, Y. Liang, M. Qiang, F. Su and T. Chen, *Langmuir*, 2019, **35**, 16900–16906.
39 U. Waiwijit, C. Chananonnawathorn, P. Eimchai, T. Bora, G. L. Hornyak and N. Nuntawong, *Appl. Surf. Sci.*, 2020, **530**, 147171.
40 R. H. Dong, T. Zhang and X. L. Feng, *Chem. Rev.*, 2018, **118**, 6189–6235.
41 Y. Shin, J. Song, D. Kim and T. Kang, *Adv. Mater.*, 2015, **27**, 4344–4350.

42 S. R. Si, W. K. Liang, Y. H. Sun, J. Huang, W. L. Ma, Z. Q. Liang, Q. L. Bao and L. Jiang, *Adv. Funct. Mater.*, 2016, **26**, 8137–8145.
43 L. P. Song, N. X. Qiu, Y. J. Huang, Q. Cheng, Y. P. Yang, H. Lin, F. M. Su and T. Chen, *Adv. Opt. Mater.*, 2020, **8**, 1902082.
44 X. Wang, S. C. Huang, S. Hu, S. Yan and B. Ren, *Nat. Rev. Phys.*, 2020, **2**, 253–271.
45 H. L. Wang, E. M. You, R. Panneerselvam, S. Y. Ding and Z. Q. Tian, *Light: Sci. Appl.*, 2021, **10**, 161.
46 Y. Ma, Y. Y. Du, Y. Chen, C. J. Gu, T. Jiang, G. D. Wei and J. Zhou, *Chem. Eng. J.*, 2020, **381**, 122710.
47 G. Serban, O. Stanasel, E. Serban and S. Bota, *Drug Des., Dev. Ther.*, 2018, **12**, 1545–1566.
48 J. Izquierdo, J. J. Santana, S. Gonzalez and R. M. Souto, *Prog. Org. Coat.*, 2012, **74**, 526–533.
49 C. Bharathi, C. S. Prasad, D. V. Bharathi, R. Shankar, V. J. Rao, R. Dandala and A. Naidu, *J. Pharm. Biomed. Anal.*, 2007, **43**, 733–740.
50 H. Yang, W. Song, J. Ji, X. Zhu, Y. Sun, R. Yang and Z. Zhang, *Appl. Surf. Sci.*, 2008, **255**, 2994–2999.
51 H. L. Zheng, S. S. Yang, J. Zhao and Z. C. Zhang, *Appl. Phys. A: Mater. Sci. Process.*, 2013, **114**, 801–808.
52 C. J. Lee, S. Y. Lee, M. R. Karim and M. S. Lee, *Spectrochim. Acta, Part A*, 2007, **68**, 1313–1319.
53 B. Liu, G. Han, Z. Zhang, R. Liu, C. Jiang, S. Wang and M. Y. Han, *Anal. Chem.*, 2012, **84**, 255–261.